Proton Diffusion Mechanism in Hydrated Barium Indate Oxides

Citation for the original published paper (version of record):

Perrichon, A., Koza, M., Evenson, Z. et al (2023). Proton Diffusion Mechanism in Hydrated Barium Indate Oxides. Chemistry of Materials, 35(17): 6713-6725.
http://dx.doi.org/10.1021/acs.chemmater.3c00754

CHEMISTRY OF MATERIALS

pubs.acs.org/cm

Article

Proton Diffusion Mechanism in Hydrated Barium Indate Oxides

Adrien Perrichon, Michael M. Koza, Zach Evenson, Bernhard Frick, Franz Demmel, Peter Fouquet, and Maths Karlsson*

Cite This: https://doi.org/10.1021/acs.chemmater.3c00754

Read Online

ACCESS | Metrics & More | Article Recommendations | Supporting Information

ABSTRACT: We report on quasielastic neutron scattering (QENS) and ab initio molecular dynamics (AIMD) simulations of the mechanism of proton diffusion in the partially and fully hydrated barium indate oxide proton conductors $Ba_2In_2O_5(H_2O)_x$ (x = 0.30 and 0.92). Structurally, these materials are featured by an intergrowth of cubic and "pseudo-cubic" layers of InO_6 octahedra, wherein two distinct proton sites, H(1) and H(2), are present. We show that the main localized dynamics of these protons can be described as rotational diffusion of O−H(1) species and H(2) proton transfers between neighboring oxygen atoms. The mean residence times of both processes are in the order of picoseconds in the two studied materials. For the fully hydrated material, $Ba_2In_2O_5(H_2O)_{0.92}$, we also reveal the presence of a third proton site, H(3), which becomes occupied upon increasing the temperature and serves as a saddle state for the interexchange between H(1) and H(2) protons. Crucially, the occupation of the H(3) site enables long-range diffusion of protons, which is highly anisotropic in nature and occurs through a two-dimensional pathway. For the partially hydrated material, $Ba_2In_2O_5(H_2O)_{0.30}$, the occupation of the H(3) site and subsequent long-range diffusion are not observed, which is rationalized by hindered dynamics of H(2) protons in the vicinity of oxygen vacancies. A comparison to state-of-the-art proton-conducting oxides, such as barium zirconate-based materials, suggests that the generally lower proton conductivity in $Ba_2In_2O_5(H_2O)_x$ is due to a large occupation of the H(1) and H(2) sites, which, in turn, means that there are few sites available for proton diffusion. This insight suggests that the chemical substitution of indium by cations with higher oxidation states offers a novel route toward higher proton conductivity because it reduces the proton site occupancy while preserving an oxygen-vacancy-free structure.

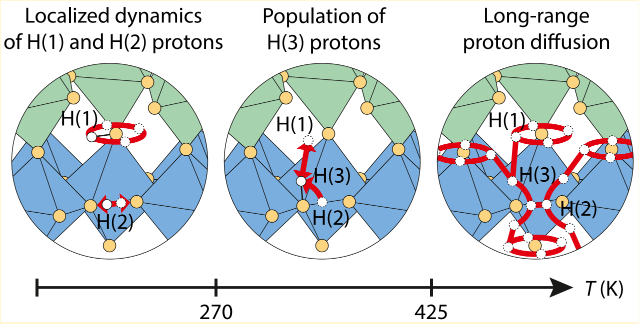

1. INTRODUCTION

Proton-conducting oxides may be applied as electrolytes in, e.g., membrane reactors[1−5] or environmentally friendly intermediate-temperature (200−500 °C) solid oxide fuel cells,[6−16] and, therefore, are gaining considerable interest for the development of a more sustainable society. Most research on proton-conducting oxides has been focused on materials exhibiting the cubic perovskite structure. Among these, yttrium-substituted barium zirconate or barium cerate with moderate substitution levels, $Ba(Zr/Ce)_{1-x}Y_xO_3H_x$ with $x \leq 0.2$,[17,18] have been the gold standard achieving the best proton conductivities at intermediate temperatures. Recently, however, high proton conductivities have been also reported in non-cubic systems,[19] such as monoclinic[20−22] and hexagonal[23−26] perovskite derivatives, oxides with palmierite[27] or scheelite[28−30] structures, and Ruddlesden−Popper phases.[21,31]

In this work, we focus on the brownmillerite-structured material barium indate oxide, $Ba_2In_2O_5$, which, structurally, is featured by an intergrowth of alternating (perovskite-like) InO_6 octahedral layers and InO_4 tetrahedral layers, in which oxygen vacancies are ordered and form one-dimensional vacancy channels (Figure 1a).[32−34] If annealed in a humid atmosphere at elevated temperatures, $Ba_2In_2O_5$ transforms into a hydrogenated, proton-conducting material, of the composition $Ba_2In_2O_5(H_2O)_x$.[35,36] During the hydration reaction, gaseous water molecules dissociate into hydroxyl groups (OH^-), which fill the former tetrahedral layers to create a structurally distorted ("pseudo-cubic") layer, and protons (H^+), which delocalize into the former, relatively undistorted ("cubic") layer. Depending on the hydration conditions, x may be tuned from 0 (nonhydrated material) to 1 (fully hydrated material). Beyond the end product that is the hydrated pseudo-cubic phase, the hydration mechanism is a complex process, as it involves a structural phase transition as well as an intermediate phase for $T \gtrsim 300$ °C.[36−40]

Previous works on the fully hydrated material have shown that at least two distinct proton sites, H(1) and H(2), are

Received: March 31, 2023
Revised: June 16, 2023

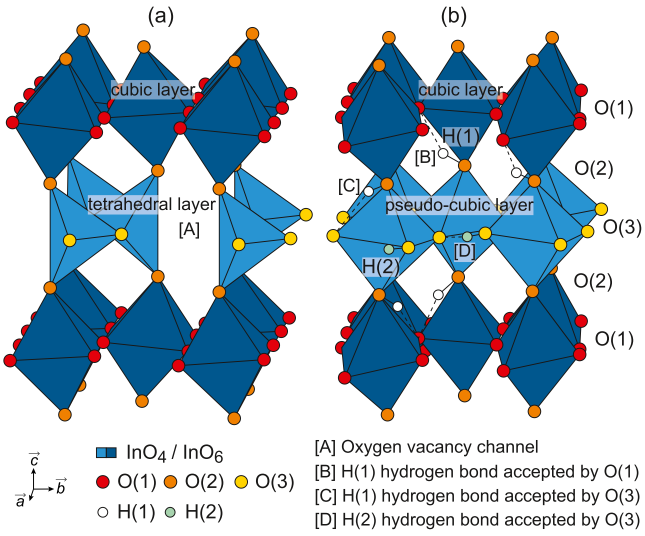

Figure 1. Schematic structure of (a) $Ba_2In_2O_5$ and (b) fully hydrated equivalent $BaInO_3H$, with the notations used in this work. Covalent bonds and hydrogen bonds are distinguished by continuous and dashed black lines, respectively. The layers formed by the $InO(1)_4O(2)_2$ octahedra, normal to $\vec{c}$, are referred to as "cubic" layers (dark blue), and the layers formed by the $InO(3)_{2-4}O(2)_2$ polyhedra as "tetrahedral" or "pseudo-cubic" layers depending on the degree of hydration (light blue).

present, see Figure 1b.[40−43] The H(1) protons form covalent bonds to the oxygen atoms connecting the two layers, O(2), and may be hydrogen bonded either to O(1) in the cubic layer or to O(3) in the pseudo-cubic layer.[44] A larger fraction of protons form relatively stronger hydrogen bonds to O(1), while the smaller fraction forms relatively weaker hydrogen bonds to O(3).[45] The H(2) protons form covalent bonds to O(3) and experience a strong hydrogen bond to an O(3) of a neighboring octahedron, with the O(3)−H···O(3) bond angle being close to 180°.[44,45] About 10% of the H(2) protons are found in configurations close to the saddle state of proton transfer along the hydrogen bond,[45] due to unusually short oxygen−oxygen separation distances, for perovskite-related oxides, of about 2.6 Å. Importantly, the number and geometry of proton environments have been found to be largely independent of the hydration level, due to a phase separation between dehydrated domains and hydrogen-rich oxygen-rich domains that maintain the pseudo-cubic structure.[36,45]

With respect to its proton-conducting properties, previous studies of $Ba_2In_2O_5(H_2O)_x$ have shown that the proton-conduction mechanism involves localized motions of protons, indicated as the diffusional rotation of O−H groups and proton transfers (jumps) between neighboring oxygen atoms, exactly like in other proton-conducting oxides.[13,46−52] In previous work, we showed using AIMD that the H(1) protons can more easily undertake rotational motions than proton transfers, whereas the opposite is true for the H(2) protons.[45] However, because the long-range proton diffusion mechanism must involve the interexchange of protons between the two sites, these two localized proton motions are insufficient to explain the proton diffusion mechanism in $Ba_2In_2O_5(H_2O)_x$. In the present work, we present experimental evidence using QENS of the main localized dynamics of the H(1) and H(2) protons. We also show that the interexchange of H(1) and H(2) protons, which enables long-range proton diffusion, is indicated by the population of a third, distinct, proton site, which leads to a highly anisotropic proton-conduction mechanism. Crucially, this process is hindered by the presence of oxygen vacancies in the structure, which explains that long-range proton diffusion is not observed in the partially hydrated material, $Ba_2In_2O_5(H_2O)_{0.30}$. Finally, we discuss these findings in relation to proton conductivities reported in related proton-conducting perovskite materials and show that, with respect to the latter, the relatively lower proton conductivity in $Ba_2In_2O_5(H_2O)_x$ is not a consequence of higher energy barriers or lower proton diffusivity but of the limited availability of vacant proton sites.

2. EXPERIMENTAL SECTION

2.1. Quasielastic Neutron Scattering. The QENS experiments were performed on three different instruments: the cold-neutron direct-geometry spectrometers TOFTOF at the Heinz Maier-Leibnitz Zentrum, Germany, and IN6 at the Institut Laue-Langevin (ILL), France, and the cold-neutron backscattering spectrometer IN16B at the ILL. The samples, $Ba_2In_2O_5(H_2O)_{0.92}$ (BIO92) and $Ba_2In_2O_5(H_2O)_{0.30}$ (BIO30), are the same samples measured with inelastic neutron scattering in ref 45, which also contains detailed information of their synthesis, hydration protocol, and laboratory characterization by thermogravimetric analysis and powder X-ray diffraction.

The measurements on TOFTOF were performed on BIO92 mounted in a flat aluminum cell sealed with an aluminum wire. Data were collected at temperatures of T = 200, 400, 450, and 485 K using an incident neutron wavelength of λ = 2.5 Å and a chopper speed of 22000 rpm, leading to an energy resolution of about 480 μeV at the elastic line, and a maximum momentum transfer of $Q \approx 4.5$ Å^{-1}. Note that the Q-ranges of 2.4−3.3 and 4.0−4.5 Å^{-1} were excluded from the data analyses due to the presence of Bragg peaks in these intervals. Data were also collected at T = 200 and 485 K using incident neutron wavelengths of λ = 5.0 Å (10 000 rpm) and 7.0 Å (8000 rpm), associated with energy resolutions of about 125 and 55 μeV, respectively. Comparison with a vanadium standard indicated that no quasielastic broadening is present at 200 K at the three resolutions. Consequently, the 200 K data were used as resolution functions in the data analysis. The measurements on IN6 were performed on both samples. The samples were mounted in flat aluminum cells sealed with a lead wire. Data were collected at T = 2, 250, 300, 350, 400, 450, and 500 K using an incident neutron wavelength of λ = 5.12 Å, which led to an energy resolution of about 90 μeV at the elastic line and gave access to the Q-range of 0.3−2.1 Å^{-1}. The T = 2 K data were used as resolution functions in the data analysis.

The measurements on IN16B were performed on both samples, which were held in the same cells as used on IN6. The incident neutron wavelength was set to λ = 6.27 Å, which, with the use of the Si(111) analyzer, led to an energy resolution of 0.75 μeV at the elastic line and a Q-range of 0.2−1.9 Å^{-1}. Elastic fixed window scans were performed upon heating to monitor the evolution of the elastic intensity from T = 20 to 500. QENS measurements were performed at T = 2, 300, 350, 400, 450, and 500 K on BIO92 and at T = 2, 300, 400, and 500 K on BIO30. The T = 2 K data were used as resolution functions in the data analysis.

Data were reduced using the Mantid software[53] for TOFTOF and IN16B and the LAMP software[54] for IN6. The fitting of the QENS spectra was performed with Mantid and in-house scripts. The measured QENS signal reflects the inelastic incoherent structure factor, $S_{\mathrm{meas.}}(Q, \hbar\omega)$, where $\hbar\omega$ is the energy transfer. Additional measurements were performed with the OSIRIS spectrometer at the ISIS Neutron and Muon Source, U.K., and with the IN11C spin-echo spectrometer at the ILL; however, these measurements did not provide any additional information about the dynamics and, therefore, are not shown.

2.2. Computational Details. The AIMD simulations were performed in the density functional theory framework using a plane-wave pseudo-potential approach as implemented in VASP

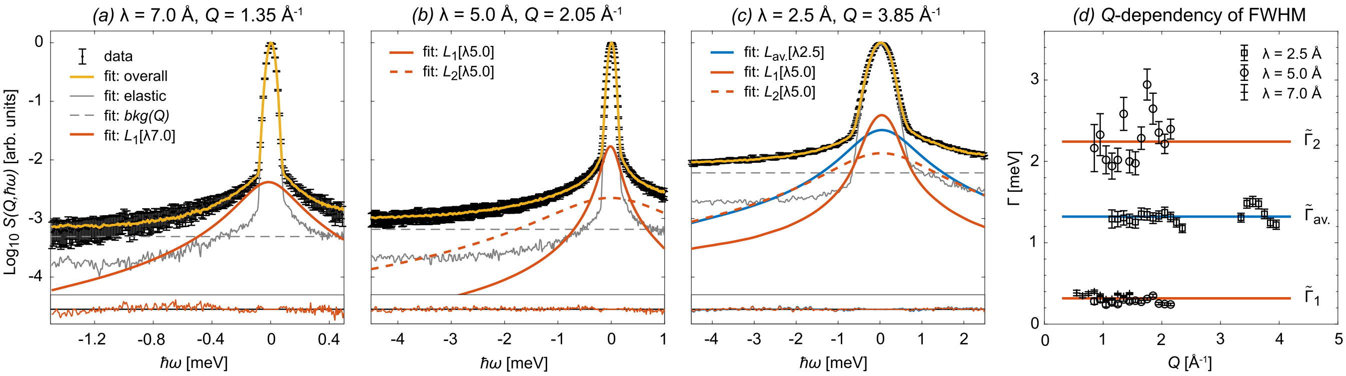

Figure 2. QENS spectra of BIO92 measured with TOFTOF at T = 485 K, with λ = 7.0 Å (a), 5.0 Å (b), and 2.5 Å (c). The QENS components are shown as full and dashed red lines for the two-Lorentzian model and a blue line for the one-Lorentzian model. Residuals are reported at the bottom of each panel. (d) Fitted values of the Γ of the Lorentzian functions and their Q-independent averages $\tilde{\Gamma}$.

5.3.[55−58] The ionic core−valence interaction is described using the projector augmented wave method[59,60] and the exchange−correlation part using the semi-local Perdew−Burke−Ernzerhof functional.[61] The structural models of $Ba_2In_2O_5(H_2O)_x$ were built considering 2 × 2 × 1 supercells with respect to the conventional brownmillerite cell, which corresponds to 8 $Ba_2In_2O_5$ units and 1−8 extra water molecules. Detailed information can be found in ref 45. The simulations were performed on the fully hydrated x = 1 (BIO100) and partially hydrated x = 0.5 (BIO50) models. The structural models were geometry-optimized considering a 1 × 1 × 2 k-point mesh for the Brillouin zone sampling.

The Verlet algorithm was used to generate the AIMD trajectories, considering a time step of dt = 0.5 fs. Only Γ-point Bloch functions were considered for the Brillouin zone sampling. The temperature was regulated using a canonical ensemble by coupling the system to a Nosé−Hoover thermostat.[62−64] Simulations were performed at T = 300 and 1200 K. The high-temperature simulations were intended to bring enough diffusion events in the limited time length of the AIMD to obtain statistically relevant information, which is a standard strategy employed with the AIMD technique.[65] Note that, despite the real material starting to dehydrate at ∼550 K, it is possible to use an unphysically high temperature of 1200 K in the simulation because the system still exhibits the correct average structure.

The structural models were thermalized by AIMD over a simulation time of 2 ps (4000 steps). Exploitable data consist of six independent sets of trajectories per model, with a length per trajectory of 8 ps (16 000 steps) at 300 K and 5 ps (10 000 steps) at 1200 K. The limited length of each simulation is a consequence of the difficulty to keep the hydrogen subsystem thermalized, given the large mass difference between barium and hydrogen and the resulting lack of overlap between the vibrational frequencies of the protons ($\hbar\omega \gtrsim$ 100 meV) and of the lattice dynamics ($\hbar\omega \lesssim$ 80 meV).[45] Nonetheless, the total trajectory lengths of 48 ps at 300 K and 30 ps at 1200 K are sufficient to obtain time-averaged structural information on the proton distribution and to characterize the geometry and jump distances of the elementary jump-diffusion motions.

Given the short and fragmented trajectories, time-dependent properties such as mean square displacements and time-correlation functions cannot be exploited to obtain diffusion coefficients and simulated QENS spectra, respectively. Instead, the AIMD is used as an exploratory tool to investigate the variety and, to some degree, the distribution of proton local environments. This is achieved, using the in-house PRM code,[66] by calculating time-averaged structural parameters and nuclear density maps. The latter were obtained by integrating, in the form of a histogram, the exploitable AIMD trajectories.

The cell parameters, and structural parameters associated with the hydrogen bonding network, obtained for BIO100 in the geometry optimization and AIMD simulations at 300 K, are reported in Tables S1 and S2 in the Supporting Information (SI). From the geometry optimization calculations, we obtain very similar parameters as the previous theoretical studies by Dervişoğlu et al. for a similar distribution of protons.[44] The agreement with experimental values is also reasonable, with about a 1.1% difference for a and b and 2.6% for c,[43] considering the complexity of the structural model, in which symmetry is reduced to P_1 from accommodating 16 protons into the supercell. The cell parameters used in the AIMD are obtained iteratively by minimizing the residual pressure on each axis at a given temperature, using as a starting point the geometry-optimized structure parameters. They have a lower agreement with the experimental cell parameters, especially for the c-axis with a difference of ∼4.1%, which is due to the lower precision of the calculation that is a necessity to run the AIMD. Besides cell parameters, covalent and hydrogen bond lengths and hydrogen bond angles obtained by AIMD are also in good agreement with previous theoretical work,[44] and in fair agreement with experimental values,[43] given the difference between the P_1 description of the AIMD and high-symmetry description from diffraction, which does not account for oxygen displacements due to the hydrogen bonding network. Beyond structural parameters, we have shown previously that the vibrational dynamics of the proton calculated by AIMD, which depend on the shape of the potential in which the proton is located, are also in excellent agreement with experimental data.[45]

3. RESULTS

3.1. Fully Hydrated Phase.

3.1.1. Main Localized Dynamics of H(1) and H(2) Protons. The fully hydrated material, BIO92, was subjected to measurements on TOFTOF, IN6, and IN16B. Figure 2a−c shows the QENS spectra of BIO92 measured on TOFTOF at T = 485 K for λ = 2.5, 5.0, and 7.0 Å, respectively, at the highest Q-value available for each wavelength. In accordance with several previous QENS studies on proton-conducting oxides,[13,46−52] under similar experimental conditions, the QENS spectra could be adequately fit by a sum of Lorentzian functions.

$$S_{\text{meas.}}(Q,\hbar\omega) = bkg(Q) + \left[a_{\text{D}}(Q)\delta(\hbar\omega) + \sum_j a_{L_j}(Q)L_j(\hbar\omega)\right] \times R(Q,\hbar\omega) \qquad (1)$$

where $\delta(\hbar\omega)$ is a Dirac function, $L_j(\hbar\omega)$ represents j Lorentzian functions that describe the quasielastic scattering and relate to localized proton motions, $bkg(Q)$ is a $\hbar\omega$-independent background, and $R(Q, \hbar\omega)$ is the instrumental resolution function. $a_D(Q)$ and $a_{L,j}(Q)$ are the elastic and quasielastic intensities, respectively.

Our analysis of the QENS spectra shows that the $\lambda = 7.0$ Å spectra can be fitted with one Lorentzian function ($L_1[\lambda7.0]$), the $\lambda = 5.0$ Å spectra can be fitted with two Lorentzian functions ($L_1[\lambda5.0]$ and $L_2[\lambda5.0]$), and the $\lambda = 2.5$ Å spectra can be fitted with one Lorentzian function ($L_{av.}[\lambda2.5]$). The widths, Γ, of all Lorentzian functions are independent of Q, which suggests that all Lorentzians reflect localized dynamics of the protons. Note that the Γ-values of $L_1[\lambda5.0]$ and $L_1[\lambda7.0]$ are found to be comparable, which indicates that they represent the same dynamical process. Therefore, the combined analyses of the $\lambda = 5.0$ Å and $\lambda = 7.0$ Å data point toward (only) two distinctly different dynamical processes. The average Γ-values for these processes are $\tilde{\Gamma}_1 = 0.32(7)$ meV and $\tilde{\Gamma}_2 = 2.2(3)$ meV (Figure 2d). These Γ values correspond to timescales of $\tau_1 \approx 4$ ps and $\tau_2 \approx 0.6$ ps, respectively. For the $\lambda = 2.5$ Å spectra, a model based on two Lorentzian functions, with the widths fixed to $\tilde{\Gamma}_1$ and $\tilde{\Gamma}_2$ (Figure 2c), as well as a fit based on only one Lorentzian function with a width of $\tilde{\Gamma}_{av.} = 1.3(2)$ meV, that is the average of $\tilde{\Gamma}_1$ and $\tilde{\Gamma}_2$, equally well fit the spectra. As for the data for $\lambda = 5.0$ Å, this suggests that two dynamical processes contribute to the $\lambda = 2.5$ Å data, yet indistinguishable due to the lower energy resolution at this relatively short neutron wavelength.

To help in the assignment of these two dynamical processes, we now consider the proton nuclear densities calculated by AIMD at 300 K for BIO100, as shown in Figure 3. For clarity, the proton nuclear densities have been projected on the (a, b)-plane and superimposed to a scheme of the initial structure of the trajectory to draw the correspondence between nuclear density spots and atomic sites. The data reveal dynamics strictly confined to the (a, b)-plane, ascribed to O(2)−H(1) rotations (up to four spots depending on statistics, marked as [A]) and O(3)−H(2)··O(3) proton transfers (up to two spots, marked as [B]). The processes are featured by a jump distance of 1.392(1) Å for the O−H(1) rotation and 0.692(3) Å for the H(2) proton transfer, which both have similar activation energies of ≲25 meV. Crucially, both processes feature mean residence periods of a few picoseconds, which match the measurable timescales on TOFTOF and, therefore, suggest that these processes are likely to correspond to localized dynamics. Further information about the observed dynamics can be extracted by our analysis of the elastic incoherent structure factor (EISF).

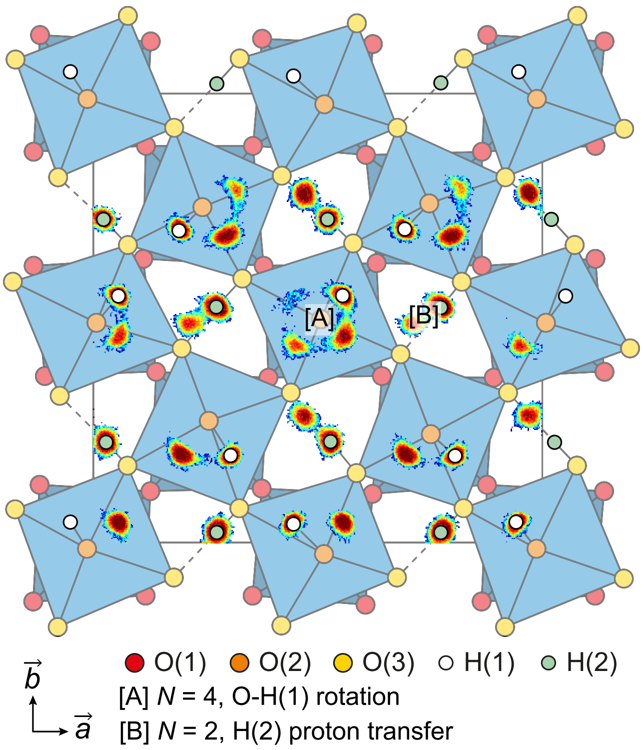

Figure 3. Structural model of BIO100 after equilibration, used as starting point of the AIMD production run, with the histogram of the proton nuclear densities at 300 K superimposed.

Figure 4 shows the EISF as determined from the neutron data at $T = 400$, 450, and 485 K (for details of the extraction of the EISF, see the SI†). Included in the figure are fits to a jump-diffusion model over two ($N = 2$) and four ($N = 4$) equivalent sites, considering an average proton site, $H_{av.}$. These models are widely used for describing the proton transfer and O−H rotational motion in proton-conducting oxides.[67] We have also included a "mixture model", that is the sum of an $N = 2$ model, reflecting O−H(1) rotations, and an $N = 4$ model, reflecting H(2) proton transfers, with the respective jump distances constrained to $d = 1.40$ Å for H(1) and 0.70 Å for H(2), as determined by the AIMD simulations. All models include a constant ϵ, which accounts for excess elastic intensity not captured by the jump-diffusion models (see the SI†) and hence represents the fraction of "immobile" protons. All models fit equally well to the experimentally determined EISF, with ϵ in the range of 80−90%; the fitting parameters are shown in Table 1. The $N = 4$ model can, however, be discarded on a chemical basis, as the fitted value of r would lead to an unphysical bond length for a hydroxyl group of 0.74−0.80 Å. The $N = 2$ model gives jump distances of an average proton in the range of $d = 1.22$−1.28 Å, which are in poor agreement with the expected jump distances of $d = 1.6$−1.9 Å for H(1) and of $d = 0.6$−0.8 Å for H(2). Therefore, the best agreement is considered to be reached with the mixture model, which suggests that the QENS signal originates from about ∼60% from H(2) proton transfers and ∼40% from O−H(1) rotations.

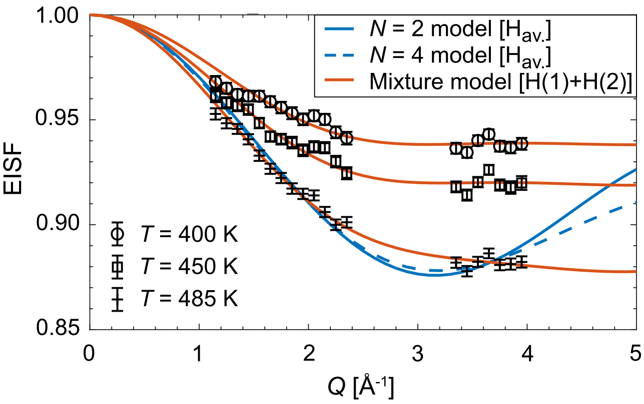

Figure 4. EISF of BIO92 calculated from the $\lambda = 2.5$ Å data at $T = 400$, 450, and 485 K, together with model functions (see text).

Figure 5 summarizes the results from the measurements on IN6. Figure 5a shows the QENS spectrum at $T = 500$ K, together with fits. Because the energy resolution and the dynamic range on IN6 and TOFTOF are comparable, similar

Table 1. Compilation of Parameters for the EISF Analysis (Figure 4)[a]

	T [K]	400	450	485
$N = 2$ model	r [Å]	0.64(2)	0.64(2)	0.61(1)
	ϵ [%]	90(3)	88(3)	82(2)
$N = 4$ model	r [Å]	0.80(2)	0.79(2)	0.74(1)
	ϵ [%]	93(3)	91(3)	88(2)
mixture model	ρ [%]	56(3)	57(3)	66(2)
	ϵ [%]	91(4)	88(3)	82(2)

[a] Jump-diffusion model over N equivalent sites placed upon a circle of radius r. For $N = 2$, the jump distance is $d = 2r$; for $N = 4$, it is $d = r\sqrt{2}$. For the mixture model, the relative contribution of the H(2) proton to the total H(1) + H(2) signal is given by the fraction ρ.

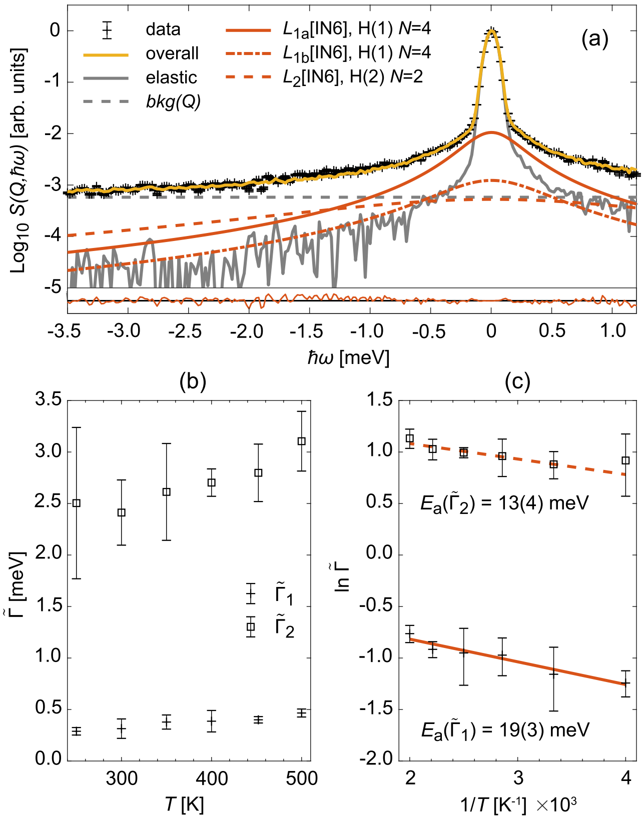

Figure 5. (a) QENS spectrum of BIO92, as measured with IN6 at T = 500 K and Q = 1.7 Å^{-1}, together with its fits. Residuals of the fits are reported at the bottom of the panel. According to the N = 4 jump-diffusion model, the Γ of the component L_{1b} is constrained to twice that of L_{1a}. (b) Fitted values of $\tilde{\Gamma}_1$ and $\tilde{\Gamma}_2$ as a function of temperature. (c) Arrhenius law derived from the temperature dependence of $\tilde{\Gamma}_1$ and $\tilde{\Gamma}_2$. Activation energies are obtained by fitting the Arrhenius law with linear functions.

quasielastic contributions can be expected in both spectra. The IN6 QENS spectra were therefore fitted with the mixture model, and the temperature dependence of the Q-averaged widths of O−H(1) rotations and H(2) proton transfers, $\tilde{\Gamma}_1$ and $\tilde{\Gamma}_2$, are shown in Figure 5b; see the SI†, for details of the fitting procedure. We observe that the O−H(1) rotation is associated with $\tilde{\Gamma}_1$ values of 0.29(4)−0.47(4) meV ($\tau_1 \approx$ 2.8−4.6 ps) and the H(2) proton transfer to $\tilde{\Gamma}_2$ values of 2.4(4)−3.1(3) meV ($\tau_2 \approx$ 0.4−0.5 ps). These values are in good agreement with the values of $\tilde{\Gamma}_1$ = 0.32(7) meV and $\tilde{\Gamma}_2$ = 2.2(3) meV measured at 485 K with TOFTOF. The temperature dependence of $\tilde{\Gamma}_1$ and $\tilde{\Gamma}_2$ follows the Arrhenius law, $\Gamma(T) = \Gamma_0 \exp(-E_a/k_BT)$, where Γ_0 is the pre-exponential factor linked to the trial frequency of the motion and E_a is the activation energy that represents the classical migration barrier for the diffusion process. The O−H(1) rotation and H(2) proton transfer take on E_a values of 19(3) and 13(4) meV, respectively (Figure 5c).

Since E_a values for the two processes are comparable, the large difference of about a factor 10 between $\tilde{\Gamma}_1$ and $\tilde{\Gamma}_2$ should be related to a difference of Γ_0, which are 0.69(6) meV for the O−H(1) rotation and 4.0(6) meV for the H(2) proton transfer. This large difference can be rationalized when considering that the trial frequency should be, in a first approximation, proportional to the potential energy surface of the proton in the direction of the diffusion motion, hence the vibrational mode of the proton. In the case of the O−H(1) rotation, this mode is the O−H wag mode in the (a, b)-plane, and in the case of the proton transfer of H(2), it is the O−H stretch mode. These modes have energies of 100 and 365 meV, respectively,[45] which qualitatively agrees with the difference in trial frequencies.

A noteworthy result of our analysis is that the most favorable dynamical process in BIO92 is the interoctahedral proton transfer of H(2) protons. Interestingly, this is in contrast to most literature data on proton-conducting oxides for which the O−H rotation motion has been generally identified as the most favorable localized proton motion.[68−70] In BIO92, it is clearly the strength and specific geometry of the hydrogen bond formed by H(2) and the close proximity of only 0.7 Å between the two H(2) sites that facilitate the proton transfer step.

3.1.2. H(3) and H(4) Proton Sites. Figure 6 shows the isotropic mean square displacement $\Delta\langle u^2\rangle_{\text{iso}}(T)$ derived from the elastic fixed window scans on IN16B according to the procedure described in the SI†. Three linear functions are necessary to account for the temperature dependence of $\Delta\langle u^2\rangle_{\text{iso}}(T)$. The low-temperature process (green line) is the contribution from the Debye−Waller factor, with $\Delta\langle u^2\rangle_{\text{iso}}(T)$ increasing in response to the activation of phonon modes of the oxygen sublattice, which thus displace the attached protons.[45] However, some contributions from O−H(1) rotations and H(2) proton transfers may be also present, given their low activation energies. Additional processes activate at about 270 and 425 K, which are distinguished by the inflection points at these temperatures. At the highest temperature, 500 K, we estimate that the contribution to

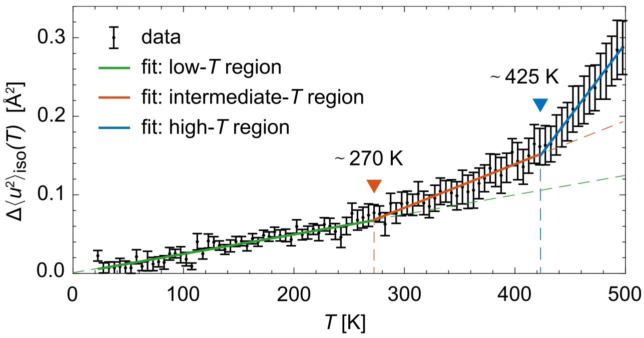

Figure 6. $\Delta\langle u^2\rangle_{\text{iso}}(T)$ for BIO92. The inflection points at about 270 and 425 K are indicated.

$\Delta\langle u^2\rangle_{\mathrm{iso}}$ is 40% from the Debye–Waller factor and 25 and 35% from the processes activating at 270 and 425 K, respectively.

Figure 7 summarizes the results from the measurements on IN16B. Figure 7a shows the QENS spectrum at T = 500 K. For temperatures $T \leq 350$ K, the QENS spectra can be adequately fitted to a single Lorentzian component (L_3[IN16B]), but for higher temperatures, two Lorentzian functions (L_3[IN16B] and L_4[IN16B]) are needed. This confirms the activation of more processes as a function of increasing temperature, as it agrees with the behavior of $\langle u^2\rangle_{\mathrm{iso}}(T)$, as shown in Figure 6.

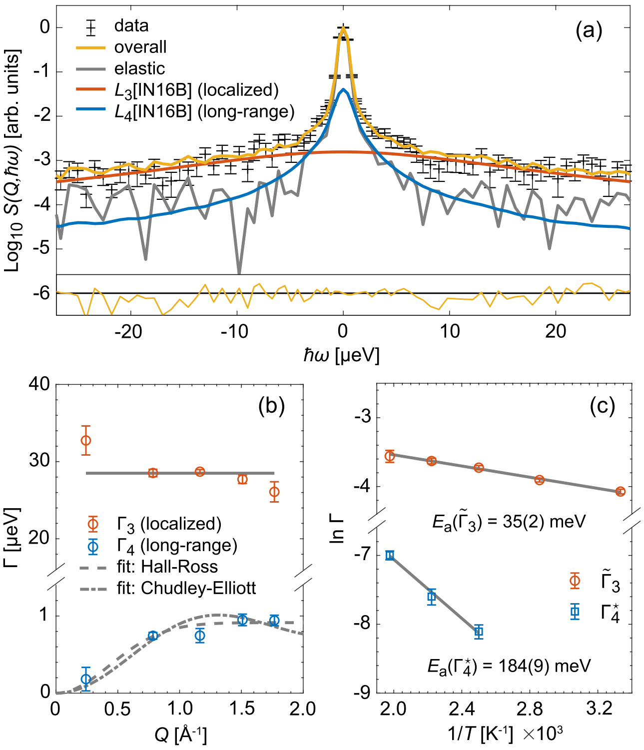

Figure 7. (a) QENS spectrum of BIO92 measured on IN16B at T = 500 K and Q = 1.7 Å^{-1}, together with its fits. Residuals of the fits are reported at the bottom of the panel. (b) Q-dependence of the widths Γ_3 and Γ_4 of the L_3[IN16B] and L_4[IN16B] functions, from the fit of the T = 500 K data. $\tilde{\Gamma}_3$ is the error-weighted average of $\Gamma_3(Q)$. The values of $\Gamma_4(Q)$ are fitted with the Hall–Ross and Chudley–Elliott models, respectively. (c) Arrhenius law derived from the temperature dependence of $\tilde{\Gamma}_3$ and the high-Q limit of Γ_4, Γ_4^*, obtained from the Hall–Ross fit. Activation energies are indicated.

For a more detailed analysis of the higher-temperature behavior, we observe that the width of L_3[IN16B] is (within error) Q-independent (Figures 7b and S4†), which thus reflects a localized proton motion. Depending on the temperature, the width takes on a value of $\tilde{\Gamma}_3$ = 17(2)–29(3) μeV ($\tau_3 \approx$ 45–77 ps), which corresponds to an E_a value of 35(2) meV (Figure 7c). Crucially, this value is about 2–3 times higher than the activation energies determined for the O–H(1) rotation (19(3) meV) and H(2) proton transfer (13(4) meV). This suggests that the dynamics reflect an additional, less favorable, localized process. Note that, due to large uncertainties, no information on the geometry of the localized motion can be extracted from the Q dependency of the quasielastic amplitude.

In order to unravel the nature of this localized process, we consider the proton nuclear densities as calculated by AIMD at 1200 K for BIO100, projected on the (a,b)-plane, and superimposed to a scheme of the structure (Figure 8).

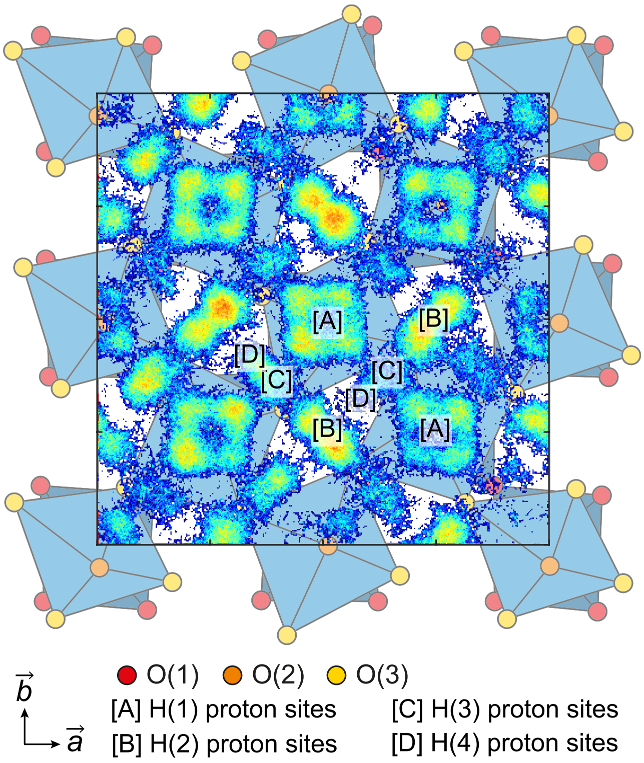

Figure 8. Structural model of BIO100. The histogram of the proton nuclear densities at 1200 K, projected on the (a, b)-plane, is superimposed.

Compared to the simulations at 300 K (Figure 3), we observe that the nuclear density spots of H(1) and H(2) (marked [A] and [B], respectively) are now more extended. Further, equivalent proton sites are more homogeneously occupied, which indicates that a higher number of diffusion events are taking place within the simulated timescale. In particular, we observe the presence of additional spots in the proton nuclear densities, marked as [C] and [D]. Site [C], hereafter referred to as H(3), corresponds to protons covalently bonded to O(3) and hydrogen bonded to O(2). It can be accessed either by O(3)–H(2) rotation out of the O(3) plane or by proton transfer of H(1) along its hydrogen bond, from O(2)–H(1)··O(3) to O(2)··H(3)–O(3). Hence, the H(3) site can be considered as a saddle point for the interexchange of protons between the H(1) and H(2) sites, and, crucially, its occupation enables long-range diffusion.

Site [D], hereafter referred to as H(4), is located in the pseudo-cubic layer and forms an O(3)–H(4)··O(3) pattern, similar to the H(2) site. It differs from the H(2) site in the geometry of the hydrogen bonding: whereas the H(2) site is characterized by interoctahedron hydrogen bonding, the H(4) site is characterized by intraoctahedron hydrogen bonding. The H(4) site can be accessed either by breaking of the H(2) hydrogen bond followed by a tilt of the O(3)–H(2) hydroxyl group in the (a, b)-plane or by a rotation from O(3)–H(3) to O(3)–H(4). It can thus be seen as an alternative path to connect the H(3) sites above and below the O(3) plane by two consecutive O–H rotations.

https://doi.org/10.1021/acs.chemmater.3c00754
Chem. Mater. XXXX, XXX, XXX−XXX

The occupation of the H(3) and H(4) sites at 1200 K is reliant on additional localized motions, which are the proton transfer motion between H(1) and H(3) and the O–H rotations from H(2) to H(3) and from H(3) to either H(2) or H(4). These are thus the higher-energy counterparts of the two main localized motions identified at 300 K. We rationalize the localized process observed on IN16B as originating from a combination of these higher-energy, additional localized motions.

3.1.3. Long-Range Proton Diffusion. Information about the long-range proton diffusion can be inferred from the proton nuclear densities, as calculated at a high temperature, $T = 1200$ K, see Figure 9. Note that only the protons initially occupying the H(1) sites at the beginning of the trajectory are included in Figure 9a. Similarly, only the protons initially at the H(2) sites are included in Figure 9b. Figure 9a,b shows that regardless of the starting position of the proton in the structure, any of the four proton sites (H(1), H(2), H(3), or H(4)) are occupied. Therefore, all protons are mobile and can occupy all sites, although there is a preference for the occupation of the H(1) and H(2) proton sites.

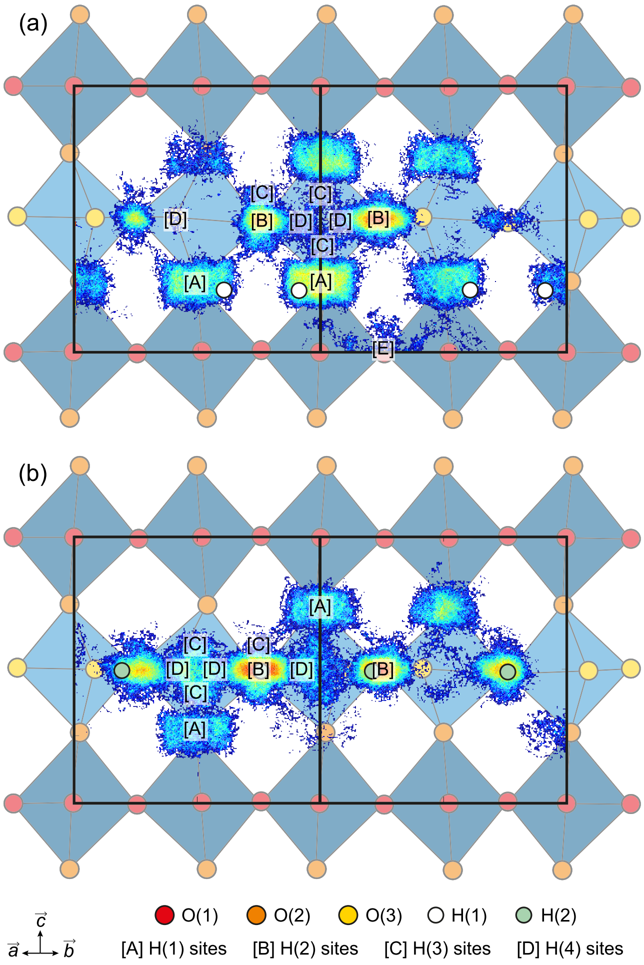

Figure 9. Structural model of BIO100. Superimposed are the histograms of the proton nuclear densities, projected on the (*ab*, *c*)-plane, obtained from integration of the AIMD trajectories at 1200 K, for the subset of H formerly on the H(1) sites (a) and for the subset of H formerly on the H(2) sites (b).

Our results show that there is a large majority of diffusion events taking place in and around the pseudo-cubic layer, which involve primarily O(2) and O(3) oxygen atoms. In fact, only a single diffusion event takes place in the O(1) layer (see [E] in Figure 9a), which is insignificant considering the high temperature of the simulation. This suggests that the long-range diffusion pathway is mainly confined in and around the O(3) planes, with an extension of the nuclear density along the *c*-axis being roughly limited to the height of the perovskite layer of ~4.3 Å (O(2)–O(2) distance along the *c*-axis). This points toward a highly anisotropic and essentially two-dimensional mechanism of long-range proton diffusion.

Long-range proton diffusion is well evident from the QENS data measured on IN16B. Specifically, the strongly *Q*-dependent behavior of width Γ_4, of the second Lorentzian (Figure 7b) for temperatures $T \geq 425$ K, is congruent with a translational, long-range, diffusion behavior. Γ_4 takes on values in the range of 0.2(2)–1.1(3) μeV, which corresponds to a characteristic timescale of the long-range dynamics of $\tau_4 \approx$ 1.2–6.6 ns. Crucially, Γ_4 can be adequately fitted to jump-diffusion models according to Chudley–Elliott[71] and Hall–Ross,[72] which represent jump-diffusion processes on an ordered lattice with a well-defined jump distance and on a disordered lattice with a distribution of jump distances, respectively, see Figures 7b and S4c–e†. Fits to the two models give comparable results, with average jump distances for the Hall–Ross model of $\langle r \rangle = 3.7(11)$ and 4.0(7) Å at 450 and 500 K, respectively, and jump distances for the Chudley–Elliott model of $\langle r \rangle = 3.2(7)$ and 3.4(6) Å at 450 K and 500 K, respectively. These values are fairly comparable to the H(1)–H(1) and H(2)–H(2) distances of ~4.2 Å, as well as with the H(1)–H(2) distance of ~3.7 Å, when considering average proton sites, but are far longer than the distance covered by a single localized diffusion event for the protons (<2 Å). This is consistent with the interpretation of a long-range diffusion mechanism that would involve combinations of localized diffusion events.

Fitting of the QENS data with respective jump-diffusion models yields diffusion coefficients for long-range proton diffusion in the range of 0.45–1.6 Å^2/ns for the Chudley–Elliott model and 0.7–2.4 Å^2/ns for the Hall–Ross model (see Table S3†). This corresponds to statistically identical activation energies of 210(31) and 212(36) meV for the Hall–Ross and Chudley–Elliott models, respectively. Alternatively, we can consider that the jump distances are temperature-independent given their uncertainties, in which case the activation energies can be extracted from the residence time or equivalently from the high-*Q* limit of Γ_4. Accordingly, activation energies of 184(9) and 187(14) meV are obtained from the temperature dependence of the saturation values Γ_4^* in the Hall–Ross (Figure 7c) and Chudley–Elliott models, respectively. Considering the different fitting approaches, the activation energy for long-range diffusion is thus estimated at 200 ± 50 meV. Such a large value of ~200 meV is compatible with the weak intensity of the L_4[IN16B] QENS signal, which only represents ca. 5% of the detected intensity at $T = 500$ K (see Figure S5b†). The four distinct proton dynamical processes identified in the BIO92 material are summarized in Table 2.

3.2. Partially Hydrated Phase. The partially hydrated material, BIO30, was subjected to measurements on IN6 and IN16B. Figure 10 shows QENS data at $T = 500$ K, as measured on IN6. In comparison to the QENS spectra of the fully hydrated material BIO92, the quasielastic scattering of BIO30 is generally weaker. This is a direct consequence of the lower

Table 2. Compilation of Proton Dynamics Data for BIO92[a]

Processes	Onset T	Timescales	E_a [meV]	Scheme
H(2) proton transfer, $N = 2$ jump diffusion model with a 0.70 Å jump distance	< 250 K	0.4–0.5 ps	13(4)	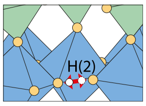
O–H(1) rotation, $N = 4$ jump diffusion model with a 1.40 Å jump distance	< 250 K	2.8–4.6 ps	19(3)	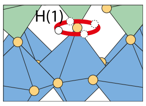
Higher energy localized motions of H(1) and H(2) that populate H(3) and H(4)	~270 K	45–77 ps	35(2)	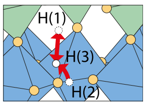
Long-range diffusion, Hall-Ross model with ~4 Å jump distances and $D = 0.7$–2.4 Å^2/ns	~425 K	1.2–6.6 ns	200(50)	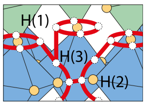

[a] Four processes, which are characterized by their spatial geometry, onset temperature, timescale, and activation energy are denoted. The panels to the right show a scheme of the dynamics.

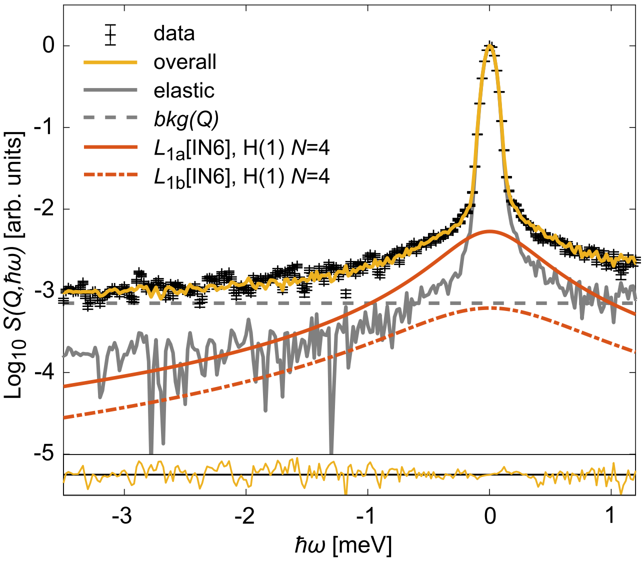

Figure 10. QENS spectrum of BIO30 measured on IN6 at T = 500 K and Q = 1.7 Å^{-1}, together with its fits. Residuals of the fits are reported at the bottom of the panel.

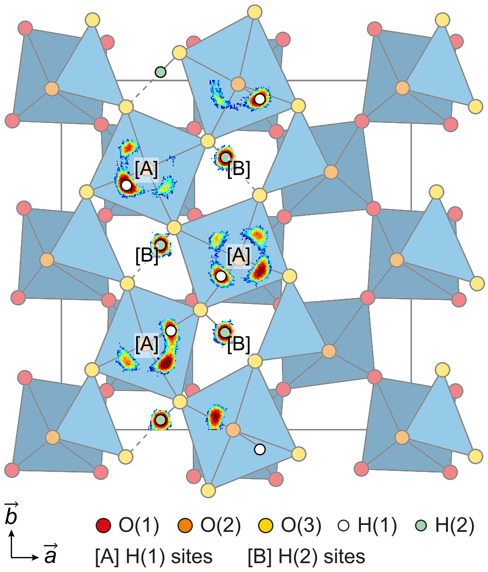

Figure 11. Structural model of BIO50 that represents the interface between the pseudo-cubic region (octahedra to the left side) and the dry, brownmillerite region (tetrahedra to the right side). The histogram of the proton nuclear densities at 300 K, projected on the (a, b)-plane, is superimposed.

hydration level. In effect, in the framework of a fit with the mixture model, the contribution of the H(2) proton transfer motion to the QENS signal, which was weak already for BIO92, is insignificant for BIO30 given the statistics of the data. Consequently, the QENS spectra of BIO30 were fitted with a model based solely on the O–H(1) rotation. This analysis showed that the O–H(1) proton dynamics are characterized by a width range of $\tilde{\Gamma}_1$ = 0.5(2)–0.7(2) meV (timescales of τ_1 = 2–3 ps) and an activation energy of E_a = 27(16) meV. Crucially, these values are similar to the ones obtained for BIO92. This suggests similar dynamics of the O–H(1) species, irrespective of the hydration level.

Figure 11 shows the proton nuclear densities from the AIMD trajectories at 300 K of BIO50. Our main interest here is the nature of the proton dynamics at the interface between the pseudo-cubic region and the dry, brownmillerite region. As compared to BIO100 (Figure 3), while we still observe a number of O–H(1) rotations (marked [A] in Figure 11), we do not observe any H(2) proton transfer events anymore ([B] in Figure 11). This suggests that the O–H(1) rotation in partially hydrated phases is not significantly impacted by the presence of nearby oxygen vacancies in the O(3) plane, and as such its activation energy should be similar to that of the fully hydrated material. The absence of the H(2) proton transfer motion in BIO50, however, suggests that this motion is hindered by the presence of oxygen vacancies in the vicinity of H(2) in partially hydrated phases. This may be due to the loss of the structural equivalence between the two H(2) sites connected by the H(2) transfer process. Indeed, H(2) sits preferentially on the side of the InO_6 octahedra and away from the InO_4 tetrahedra.

Figure 12 shows $\Delta\langle u^2\rangle_{iso}(T)$ for BIO30, as measured on IN16B. At variance with BIO92, $\Delta\langle u^2\rangle_{iso}(T)$ increases linearly all the way up to T = 500 K. This suggests that the loss of

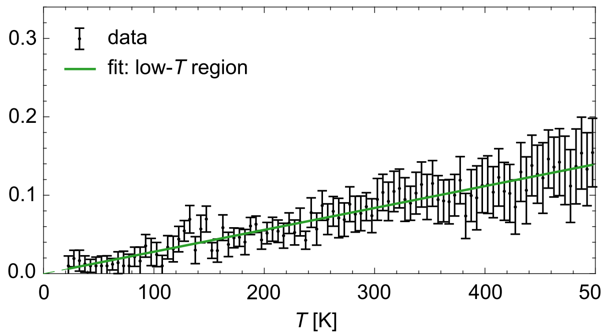

Figure 12. $\Delta\langle u^2\rangle_{\text{iso}}$ for BIO30, as measured on IN16B. The linear increase with temperature suggests the gradual activation of only vibrational dynamics (see text).

elastic intensity is solely due to the Debye−Waller factor, which is consistent with the absence of significant QENS broadening at any measured temperature. This signals the absence of diffusion processes observed in the time window of IN16B, or that such a dynamics are too weak to be observed here.

4. DISCUSSION

By bringing together the results from the QENS experiments and AIMD simulations, we can now understand several new features pertaining to the mechanism of proton diffusion in barium indate oxide proton conductors. A key result is the unraveling of a third proton site, H(3), that acts as a saddle state for the interexchange of H(1) and H(2) protons, enabling long-range proton diffusion in the fully hydrated material.

As a preliminary remark, we point out that two distinct temperature regimes have been observed by QENS in cubic perovskite proton conductors,[73] with a transition temperature usually close to the onset of dehydration, $T \approx 550$ K. The activation energies for long-range proton diffusion are higher in the high-temperature regime, where proton diffusion is discussed as solely thermally activated, than those in the low-temperature regime, where proton diffusion is discussed as phonon-mediated.

While the activation energies for O−H(1) rotations and H(2) proton transfers are comparable to those reported for localized proton diffusion in cubic-structured, proton-conducting oxides,[46,50,52,74] the activation energy for long-range diffusion of 200(50) meV in BIO92 is 2−5 times larger than that reported by QENS in the phonon-mediated regime in related cubic perovskites, with for instance ∼40 meV in $BaZr_{0.9}In_{0.1}O_3H_{0.1}$ and $BaZr_{0.9}Y_{0.1}O_3H_{0.1}$ or ∼110 meV in $BaZr_{0.8}In_{0.2}O_3H_{0.2}$.[51,73] Note that in the thermally activated diffusion regime at a higher temperature, activation energies for long-range diffusion measured by QENS in perovskite-related proton conductors are generally higher, in the range of 0.25−0.6 eV.[74−79]

As the temperatures considered here fall in the phonon-mediated diffusion regime, a tentative explanation for the higher energy barrier in BIO92 than in cubic perovskite proton conductors could be a less favorable proton−phonon interaction to promote long-range diffusion. Indeed, the two main localized motions, the O−H(1) rotation and the H(2) proton transfer, are both within the (a, b)-plane. Conversely, the localized motions that are required to populate H(3) and enable long-range diffusion have a large component in the c-direction. Regarding the role of the phonon modes in promoting diffusion processes, it is mainly the contribution from the low-energy modes with large atomic displacements that is significant.[80] The large majority of the low-energy phonon modes in the brownmillerite phase have motions within the (a, b)-plane.[41] Indeed, the first phonon mode polarized along c has a frequency of $\hbar\omega = 22$ meV (180 cm^{-1}), while there are 14 phonon modes polarized in the (a,b)-plane with lower energy, with the lowest optic phonon mode at 7.6 meV (61 cm^{-1}).[41] We can thus surmise that the proton−phonon interaction is mainly favorable to motions and elementary diffusion processes in the (a, b)-plane and, thus, that the counterpart motions that populate H(3) and enable proton interexchange and long-range proton diffusion are, in comparison, less promoted by phonon modes.

A similar trend, although less pronounced, is observed in the activation energies determined by impedance spectroscopy for proton conductivity in the bulk of the grains. Indeed, a value of ∼0.6 eV is obtained for an epitaxial thin film of barium indate under a wet atmosphere,[81] while smaller values are obtained for proton-conducting perovskites, with for instance 0.46−0.47 eV in Y-doped $BaZrO_3$.[73,82] Note that the conductivity values and thus the activation energies determined by QENS and impedance spectroscopy are not directly comparable. Indeed, conductivity values are generally significantly different, and the activation energies obtained from impedance spectroscopy are generally 2−10 times larger than the ones determined by QENS. This is because of fundamental differences, as QENS only accounts for proton self-diffusion over length scales that correspond to distances of a few unit cells, while IS has a macroscopic view of the material and contains contributions beyond proton self-diffusion.

Besides the difference in activation energy for long-range proton diffusion, we also note a clear difference in regard to the value of the macroscopic proton conductivity between hydrated barium indate and proton-conducting perovskites. Specifically, we note that the proton conductivities obtained from impedance spectroscopy measurements of $Ba_2In_2O_5(H_2O)_x$ are 1−3 orders of magnitude lower than those in the best proton-conducting perovskites, such as Y-doped $BaZrO_3$.[81−85] However, for the proton diffusion coefficients as determined by QENS, the values for different relevant proton conductors are similar. For instance, the related material $BaZr_{1-x}In_xO_{3-x/2}$ exhibits proton diffusion coefficients of 1−3 Å^2/ns,[51] which are within the same range as observed here for BIO92 (0.45−2.4 Å^2/ns). This indicates that at the nanometer length scale, there are no fundamental differences between the proton mobility in hydrated barium indate and proton-conducting perovskites.

The large difference in proton conductivities measured by impedance spectroscopy between $Ba_2In_2O_5(H_2O)_x$ and proton-conducting perovskites, if not originating from the difference in activation energy and/or proton diffusion coefficient, may then originate from a difference in the number of charge carriers, even though the concentrations of protons are similar in the respective systems. This would represent the case when a significant portion of the protons are unable to diffuse to the H(3) site within the probed timescale. This could happen if (i) the dynamics of the H(2) protons are hindered by the presence of nearby oxygen vacancies or (ii) there is a limited availability of empty proton sites to which the protons can jump. In a simplified description of BIO100, we note that there are two H(1) proton sites per H(1) proton and one H(2) proton site per H(2) proton. Hence, the fractional occupation of the proton sites, i.e., the total number of protons over the combined H(1) and H(2) sites, is 2/3 ≈ 0.67. This may be compared to the cubic-structured $BaZr_{0.8}M_{0.2}O_3H_{0.2}$, for which the fractional occupation of the proton sites is only 0.20/3 ≈ 0.067.

While the high fractional occupation for BIO100 may not hinder the O−H(1) rotation or the H(2) proton transfer, they may however severely limit the processes that populate H(3). Indeed, the H(3) site may not be available to receive a proton following a diffusion event from the H(1) or H(2) site, which we can qualitatively evaluate based on a simplified model of the structure. For instance, it is unlikely for the H(3) site to be occupied following a proton transfer from H(1) if the O(3) oxygen is already covalently bonded to H(2), which is a 50% probability (half of the O(3) are covalently bonded to H(2), the other half are acceptor of the hydrogen bond of H(2)). Similarly, a proton transfer from H(1) to O(3) is unlikely if one next-neighbor H(1) is oriented toward H(3), which is a 0.5 × 0.25 = 12.5% probability, thus resulting in a 0.5 × 0.875 ≈ 44% probability of finding the H(3) site available. The same calculation, for the rotation from H(2), considering that both next-neighbor H(1) sites cannot be simultaneously occupied nor does any next-neighbor H(1) proton oriented toward H(3), give an H(3) site availability of 62.5%. Despite its simplicity, such qualitative evaluation shows how a large fractional occupation of the proton sites may be detrimental for high proton conductivity.

Beyond the H(3) site availability, it is the sequential nature of the long-range proton diffusion mechanism that is problematic in $Ba_2In_2O_5(H_2O)_x$. Indeed, a proton occupying the H(3) site can only diffuse further if the next site is available, which is a lower probability than finding an available site where the proton originated. The lack of availability of empty sites and the lower probability for consecutive diffusion events than for "back-diffusion" are known problems that were for instance identified in the $SrVO_2H$ hydride-ion conductor, where the hydride ion has a higher probability to diffuse back to its previously occupied site than forward, due to a lack of oxygen vacancies.[86]

The straightforward solution to reduce the fractional occupation of the proton sites would be to reduce the number of protons in the structure. Unfortunately, this cannot be achieved by dehydrating the material. Indeed, beyond the discussion on partially hydrated phases, we have shown that regardless of the hydration level, protons are mainly found in proton-rich oxygen-vacancy-free regions that preserve the fully hydrated stoichiometry.[45] A strategy to preserve an oxygen-vacancy-free structure while reducing the number of protons could be to partially substitute indium atoms with tetravalent or pentavalent cations. For instance, dehydrated vanadium-substituted barium indate still displays the brownmillerite structure at moderate substitution content (≤20%) and shows under a moist Ar atmosphere about an order of magnitude increase in total conductivity compared to pristine barium indate.[85] Similarly, moderate substitution by titanium (≤20%)[87] and additional elements,[88] or high substitution by vanadium (≤40%),[85] has been shown to stabilize the high-temperature tetragonal structure of barium indate and improve protonic conductivities.

5. CONCLUSIONS

To conclude, we have performed a combined QENS and AIMD study of the proton dynamics in the partially and fully hydrated barium indate proton conductors $Ba_2In_2O_5(H_2O)_x$ (x = 0.30 and 0.92). Structurally, these materials are featured by an intergrowth of cubic and "pseudo-cubic" layers of InO_6 octahedra, wherein two distinct proton sites, H(1) and H(2), are present. The results show that the main localized dynamics of protons can be described as rotational diffusion of O−H(1) species and H(2) proton transfers between neighboring oxygen atoms, both with mean residence periods on the order of picoseconds, in both materials. For the fully hydrated material, $Ba_2In_2O_5(H_2O)_{0.92}$, we also reveal the presence of a third proton site, H(3), which becomes occupied upon increasing the temperature, serves as a saddle state for the interexchange between H(1) and H(2) protons, and leads to long-range proton diffusion on the nanosecond timescale. In comparison, the partially hydrated material $Ba_2In_2O_5(H_2O)_{0.30}$ does not show the occupation of the H(3) proton site, as a result of hindered dynamics of H(2) protons due to the vicinity of oxygen vacancies, and, hence, shows no long-range proton diffusion. The lower macroscopic proton conductivity in hydrated barium indate oxides than that in related materials, such as In-doped $BaZrO_3$-based proton conductors, despite showing comparable activation energies, is rationalized by the lack of availability of proton sites. This issue may be alleviated by the chemical substitution of indium by cations with higher oxidation states, to reduce the number of protons while preserving an oxygen-vacancy-free structure.

■ ASSOCIATED CONTENT

Supporting Information

The Supporting Information is available free of charge at https://pubs.acs.org/doi/10.1021/acs.chemmater.3c00754.

Structural parameters from AIMD; EISF analysis procedure and validation; EFWS analysis procedure; and QENS fit results (PDF)

■ AUTHOR INFORMATION

Corresponding Author

Maths Karlsson − *Department of Chemistry and Chemical Engineering, Chalmers University of Technology, SE-412 96 Göteborg, Sweden;* orcid.org/0000-0002-2914-6332; Email: maths.karlsson@chalmers.se

Authors

Adrien Perrichon − *Department of Chemistry and Chemical Engineering, Chalmers University of Technology, SE-412 96 Göteborg, Sweden;* Present Address: ISIS Facility, Rutherford Appleton Laboratory, Chilton, Didcot OX11 0QX, Oxfordshire, U.K

Michael M. Koza − *Institut Laue-Langevin, 38042 Grenoble Cedex 9, France*

Zach Evenson − *Heinz Maier-Leibnitz Zentrum and Physik Department, Technische Universität München, Garching 85748, Germany*

Bernhard Frick − *Institut Laue-Langevin, 38042 Grenoble Cedex 9, France*

Franz Demmel − *ISIS Facility, Rutherford Appleton Laboratory, Chilton, Didcot OX11 0QX Oxfordshire, U.K.*

Peter Fouquet − *Institut Laue-Langevin, 38042 Grenoble Cedex 9, France;* orcid.org/0000-0002-5542-0059

Complete contact information is available at: https://pubs.acs.org/10.1021/acs.chemmater.3c00754

Notes

The authors declare no competing financial interest.

■ ACKNOWLEDGMENTS

M.K. acknowledges support from the Swedish Research Council (Grant Nos. 2010-3519 and 2011-4887) and the Swedish Energy Agency (Grant No. 48712-1). The Institut Laue-Langevin, the Heinz Maier-Leibnitz Zentrum, and the ISIS Neutron and Muon Source are thanked for access to neutron beam facilities. Data from the ILL measurements are available in open access.[89] Simulations were performed on resources provided by the Swedish National Infrastructure for Computing (SNIC) at PDC Center for High Performance Computing (PDC-HPC). Seikh M. H. Rahman, Chalmers University of Technology, is thanked for the preparation of the samples.

■ REFERENCES

(1) Malerød-Fjeld, H.; Clark, D.; Yuste-Tirados, I.; Zanón, R.; Catalán-Martinez, D.; Beeaff, D.; Morejudo, S. H.; Vestre, P. K.; Norby, T.; Haugsrud, R.; Serra, J. M.; Kjølseth, C. Thermo-Electrochemical Production of Compressed Hydrogen From Methane With Near-Zero Energy Loss. *Nat. Energy* **2017**, *2*, 923−931.

(2) Morejudo, S. H.; Zanón, R.; Escolástico, S.; Yuste-Tirados, I.; Malerød-Fjeld, H.; Vestre, P. K.; Coors, W. G.; Martínez, A.; Norby, T.; Serra, J. M.; Kjølseth, C. Direct Conversion of Methane to Aromatics in a Catalytic Co-Ionic Membrane Reactor. *Science* **2016**, *353*, 563−566.

(3) Iwahara, H.; Esaka, T.; Uchida, H.; Maeda, N. Proton Conduction in Sintered Oxides and its Application to Steam Electrolysis for Hydrogen Production. *Solid State Ionics* **1981**, *3*−*4*, 359−363.

(4) Sakai, T.; Matsushita, S.; Matsumoto, H.; Okada, S.; Hashimoto, S.; Ishihara, T. Intermediate Temperature Steam Electrolysis Using Strontium Zirconate-Based Protonic Conductors. *Int. J. Hydrogen Energy* **2009**, *34*, 56−63.

(5) Matsumoto, H.; Shimura, T.; Iwahara, H.; Higuchi, T.; Yashiro, K.; Kaimai, A.; Kawada, T.; Mizusaki, J. Hydrogen Separation Using Proton-Conducting Perovskites. *J. Alloys Compd.* **2006**, *408*−*412*, 456−462.

(6) Coduri, M.; Karlsson, M.; Malavasi, L. Structure−Property Correlation in Oxide-Ion and Proton Conductors for Clean Energy Applications: Recent Experimental and Computational Advancements. *J. Mater. Chem. A* **2022**, *10*, 5082−5110.

(7) Duan, C.; Tong, J.; Shang, M.; Nikodemski, S.; Sanders, M.; Ricote, S.; Almansoori, A.; O'Hayre, R. Readily Processed Protonic Ceramic Fuel Cells With High Performance at Low Temperatures. *Science* **2015**, *349*, 1321−1326.

(8) Kilner, J. A.; Burriel, M. Materials for Intermediate-Temperature Solid-Oxide Fuel Cells. *Annu. Rev. Mater. Res.* **2014**, *44*, 365−393.

(9) Malavasi, L.; Fisher, C. A. J.; Islam, M. S. Oxide-Ion and Proton Conducting Electrolyte Materials for Clean Energy Applications: Structural and Mechanistic Features. *Chem. Soc. Rev.* **2010**, *39*, 4370−4387.

(10) Fabbri, E.; Pergolesi, D.; Traversa, E. Materials Challenges Toward Proton-Conducting Oxide Fuel Cells: A Critical Review. *Chem. Soc. Rev.* **2010**, *39*, 4355−4369.

(11) Kreuer, K.-D.; Paddison, S. J.; Spohr, E.; Schuster, M. Transport in Proton Conductors for Fuel-Cell Applications: Simulations, Elementary Reactions, and Phenomenology. *Chem. Rev.* **2004**, *104*, 4637−4678.

(12) Norby, T.; Widerøe, M.; Glöckner, R.; Larring, Y. Hydrogen in Oxides. *Dalton Trans.* **2004**, *19*, 3012−3018.

(13) Kreuer, K. Proton-Conducting Oxides. *Annu. Rev. Mater. Res.* **2003**, *33*, 333−359.

(14) Norby, T. Solid-State Protonic Conductors: Principles, Properties, Progress and Prospects. *Solid State Ionics* **1999**, *125*, 1−11.

(15) Kreuer, K. On the Development of Proton Conducting Materials for Technological Applications. *Solid State Ionics* **1997**, *97*, 1−15.

(16) Iwahara, H.; Yajima, T.; Hibino, T.; Ozaki, K.; Suzuki, H. Protonic Conduction in Calcium, Strontium and Barium Zirconates. *Solid State Ionics* **1993**, *61*, 65−69.

(17) Kochetova, N.; Animitsa, I.; Medvedev, D.; Demin, A.; Tsiakaras, P. Recent Activity in the Development of Proton-Conducting Oxides for High-Temperature Applications. *RSC Adv.* **2016**, *6*, 73222−73268.

(18) Medvedev, D.; Murashkina, A.; Pikalova, E.; Demin, A.; Podias, A.; Tsiakaras, P. $BaCeO_3$: Materials Development, Properties and Application. *Prog. Mater. Sci.* **2014**, *60*, 72−129.

(19) Fop, S. Solid Oxide Proton Conductors Beyond Perovskites. *J. Mater. Chem. A* **2021**, *9*, 18836−18856.

(20) Fuller, C. A.; Blom, D. A.; Vogt, T.; Evans, I. R.; Evans, J. S. O. Oxide Ion and Proton Conductivity in a Family of Highly Oxygen-Deficient Perovskite Derivatives. *J. Am. Chem. Soc.* **2022**, *144*, 615−624.

(21) Zhou, Y.; Shiraiwa, M.; Nagao, M.; Fujii, K.; Tanaka, I.; Yashima, M.; Baque, L.; Basbus, J. F.; Mogni, L. V.; Skinner, S. J. Protonic Conduction in the $BaNdInO_4$ Structure Achieved by Acceptor Doping. *Chem. Mater.* **2021**, *33*, 2139−2146.

(22) Fuller, C. A.; Berrod, Q.; Frick, B.; Johnson, M. R.; Avdeev, M.; Evans, J. S. O.; Evans, I. R. Oxide Ion and Proton Conductivity in Highly Oxygen-Deficient Cubic Perovskite $SrSc_{0.3}Zn_{0.2}Ga_{0.5}O_{2.4}$. *Chem. Mater.* **2020**, *32*, 4347−4357.

(23) Murakami, T.; Avdeev, M.; Morikawa, R.; Hester, J. R.; Yashima, M. High Proton Conductivity in β-Ba_2ScAlO_5 Enabled by Octahedral and Intrinsically Oxygen-Deficient Layers. *Adv. Funct. Mater.* **2023**, *33*, No. 2206777.

(24) Murakami, T.; Hester, J. R.; Yashima, M. High Proton Conductivity in $Ba_5Er_2Al_2ZrO_{13}$, a Hexagonal Perovskite-Related Oxide with Intrinsically Oxygen-Deficient Layers. *J. Am. Chem. Soc.* **2020**, *142*, 11653−11657.

(25) Fop, S.; McCombie, K. S.; Wildman, E. J.; Skakle, J. M. S.; Irvine, J. T. S.; Connor, P. A.; Savaniu, C.; Ritter, C.; Mclaughlin, A. C. High Oxide Ion and Proton Conductivity in a Disordered Hexagonal Perovskite. *Nat. Mater.* **2020**, *19*, 752−757.

(26) Wind, J.; Mole, R. A.; Yu, D.; Avdeev, M.; Ling, C. D. Hydration Mechanisms and Proton Conduction in the Mixed Ionic−Electronic Conductors $Ba_4Nb_2O_9$ and $Ba_4Ta_2O_9$. *Chem. Mater.* **2018**, *30*, 4949−4958.

(27) Fop, S.; Dawson, J. A.; Tawse, D. N.; Skellern, M. G.; Skakle, J. M. S.; Mclaughlin, A. C. Proton and Oxide Ion Conductivity in Palmierite Oxides. *Chem. Mater.* **2022**, *34*, 8190−8197.

(28) Norby, T.; Magrasó, A. On the Development of Proton Ceramic Fuel Cells Based on Ca-Doped $LaNbO_4$ as Electrolyte. *J. Power Sources* **2015**, *282*, 28−33.

(29) Haugsrud, R.; Norby, T. Proton Conduction in Rare-Earth Ortho-Niobates and Ortho-Tantalates. *Nat. Mater.* **2006**, *5*, 193−196.

(30) Haugsrud, R.; Norby, T. High-Temperature Proton Conductivity in Acceptor-Doped $LaNbO_4$. *Solid State Ionics* **2006**, *177*, 1129−1135.

(31) Shiraiwa, M.; Kido, T.; Fujii, K.; Yashima, M. High-Temperature Proton Conductors Based on the (110) Layered Perovskite $BaNdScO_4$. *J. Mater. Chem. A* **2021**, *9*, 8607−8619.

(32) Jayaraman, V.; Magrez, A.; Caldes, M.; Joubert, O.; Ganne, M.; Piffard, Y.; Brohan, L. Characterization of Perovskite Systems Derived From $Ba_2In_2O_5\square$: Part I: The Oxygen-Deficient $Ba_2In_{2(1-x)}Ti_{2x}O_{5+x}\square_{1-x}$ ($0 \leq x \leq 1$) Compounds. *Solid State Ionics* **2004**, *170*, 17−24.

(33) Speakman, S. A.; Richardson, J. W.; Mitchell, B. J.; Misture, S. T. In-Situ Diffraction Study of $Ba_2In_2O_5$. *Solid State Ionics* **2002**, *149*, 247−259.

(34) Berastegui, P.; Hull, S.; García-García, F.; Eriksson, S.-G. The Crystal Structures, Microstructure and Ionic Conductivity of $Ba_2In_2O_5$ and $Ba(In_xZr_{1-x})O_{3-x/2}$. *J. Solid State Chem.* **2002**, *164*, 119−130.

(35) Fischer, W.; Reck, G.; Schober, T. Structural Transformation of the Oxygen and Proton Conductor $Ba_2In_2O_5$ in Humid Air: an In-Situ X-Ray Powder Diffraction Study. *Solid State Ionics* **1999**, *116*, 211−215.

(36) Schober, T.; Friedrich, J.; Krug, F. Phase Transition in the Oxygen and Proton Conductor $Ba_2In_2O_5$ in Humid Atmospheres Below 300°C. *Solid State Ionics* **1997**, *99*, 9−13.

(37) Schober, T.; Friedrich, J. The Oxygen and Proton Conductor $Ba_2In_2O_5$: Thermogravimetry of Proton Uptake. *Solid State Ionics* **1998**, *113-115*, 369−375.

(38) Fisher, C.; Islam, M. Defect, Protons and Conductivity in Brownmillerite-Structured $Ba_2In_2O_5$. *Solid State Ionics* **1999**, *118*, 355−363.

(39) Islam, M.; Davies, R.; Fisher, C.; Chadwick, A. Defects and Protons in the $CaZrO_3$ Perovskite and $Ba_2In_2O_5$ Brownmillerite: Computer Modelling and EXAFS Studies. *Solid State Ionics* **2001**, *145*, 333−338.

(40) Bielecki, J.; Parker, S. F.; Mazzei, L.; Börjesson, L.; Karlsson, M. Structure and Dehydration Mechanism of the Proton Conducting Oxide $Ba_2In_2O_5(H_2O)_x$. *J. Mater. Chem. A* **2016**, *4*, 1224−1232.

(41) Bielecki, J.; Parker, S. F.; Ekanayake, D.; Rahman, S. M. H.; Börjesson, L.; Karlsson, M. Short-Range Structure of the Brownmillerite-Type Oxide $Ba_2In_2O_5$ and its Hydrated Proton-Conducting Form $BaInO_3H$. *J. Mater. Chem. A* **2014**, *2*, 16915−16924.

(42) Martinez, J.-R.; Mohn, C. E.; Stølen, S.; Allan, N. L. $Ba_2In_2O_4(OH)_2$: Proton Sites, Disorder and Vibrational Properties. *J. Solid State Chem.* **2007**, *180*, 3388−3392.

(43) Jayaraman, V.; Magrez, A.; Caldes, M.; Joubert, O.; Taulelle, F.; Rodriguez-Carvajal, J.; Piffard, Y.; Brohan, L. Characterization of Perovskite Systems Derived from $Ba_2In_2O_5$□: Part II: The Proton Compounds $Ba_2In_{2(1-x)}Ti_{2x}O_{4+2x}(OH)_y$ [$0\leq x\leq 1$; $y\leq 2(1\text{-}x)$]. *Solid State Ionics* **2004**, *170*, 25−32.

(44) Dervişoğlu, R.; Middlemiss, D. S.; Blanc, F.; Lee, Y.-L.; Morgan, D.; Grey, C. P. Joint Experimental and Computational ^{17}O and ^{1}H Solid State NMR Study of $Ba_2In_2O_4(OH)_2$ Structure and Dynamics. *Chem. Mater.* **2015**, *27*, 3861−3873.

(45) Perrichon, A.; Jiménez-Ruiz, M.; Mazzei, L.; Rahman, S. M. H.; Karlsson, M. Local Structure and Vibrational Dynamics of Proton Conducting $Ba_2In_2O_5(H_2O)_x$. *J. Mater. Chem. A* **2019**, *7*, No. 17626.

(46) Karlsson, M.; Matic, A.; Engberg, D.; Björketun, M. E.; Koza, M. M.; Ahmed, I.; Wahnström, G.; Börjesson, L.; Eriksson, S. G. Quasielastic Neutron Scattering of Hydrated $BaZr_{0.90}A_{0.10}O_{2.95}$ (A=Y and Sc). *Solid State Ionics* **2009**, *180*, 22−28.

(47) Karlsson, M.; Matic, A.; Zanghellini, E.; Ahmed, I. Temperature-Dependent Infrared Spectroscopy of Proton-Conducting Hydrated Perovskite $BaIn_xZr_{1-x}O_{3-x/2}$ (x = 0.10−0.75). *J. Phys. Chem. C* **2010**, *114*, 6177−6181.

(48) Karlsson, M.; Engberg, D.; Björketun, M. E.; Matic, A.; Wahnström, G.; Sundell, P. G.; Berastegui, P.; Ahmed, I.; Falus, P.; Farago, B.; Börjesson, L.; Eriksson, S. Using Neutron Spin-Echo to Investigate Proton Dynamics in Proton-Conducting Perovskites. *Chem. Mater.* **2010**, *22*, 740−742.

(49) Noferini, D.; Koza, M. M.; Fouquet, P.; Nilsen, G. J.; Kemei, M. C.; Rahman, S. M. H.; Maccarini, M.; Eriksson, S.; Karlsson, M. Proton Dynamics in Hydrated $BaZr_{0.9}M_{0.1}O_{2.95}$ (M = Y and Sc) Investigated With Neutron Spin—Echo. *J. Phys. Chem. C* **2016**, *120*, 13963−13969.

(50) Noferini, D.; Koza, M. M.; Karlsson, M. Localized Proton Motions in Acceptor-Doped Barium Zirconates. *J. Phys. Chem. C* **2017**, *121*, 7088−7093.

(51) Noferini, D.; Frick, B.; Koza, M. M.; Karlsson, M. Proton Jump Diffusion Dynamics in Hydrated Barium Zirconates Studied by High-Resolution Neutron Backscattering Spectroscopy. *J. Mater. Chem. A* **2018**, *6*, 7538−7546.

(52) Noferini, D.; Koza, M. M.; Rahman, S. M. H.; Evenson, Z.; Nilsen, G. J.; Eriksson, S.; Wildes, A. R.; Karlsson, M. Role of the Doping Level in Localized Proton Motions in Acceptor-Doped Barium Zirconate Proton Conductors. *Phys. Chem. Chem. Phys.* **2018**, *20*, 13697−13704.

(53) Arnold, O.; et al. Mantid - Data Analysis and Visualization Package for Neutron Scattering and μ SR Experiments. *Nucl. Instrum. Methods Phys. Res., Sect. A* **2014**, *764*, 156−166.

(54) Richard, D.; Ferrand, M.; Kearley, G. J. Analysis and Visualisation of Neutron-Scattering Data. *J. Neutron Res.* **1996**, *4*, 33−39.

(55) Kresse, G.; Hafner, J. *Ab initio* Molecular Dynamics for Open-Shell Transition Metals. *Phys. Rev. B* **1993**, *48*, 13115−13118.

(56) Kresse, G.; Hafner, J. *Ab initio* Molecular-Dynamics Simulation of the Liquid-Metal-Amorphous-Semiconductor Transition in Germanium. *Phys. Rev. B* **1994**, *49*, 14251−14269.

(57) Kresse, G.; Furthmüller, J. Efficiency of Ab-Initio Total Energy Calculations for Metals and Semiconductors Using a Plane-Wave Basis Set. *Comput. Mater. Sci.* **1996**, *6*, 15−50.

(58) Kresse, G.; Furthmüller, J. Efficient Iterative Schemes for *Ab Initio* Total-Energy Calculations Using a Plane-Wave Basis Set. *Phys. Rev. B* **1996**, *54*, 11169−11186.

(59) Blöchl, P. E. Projector Augmented-Wave Method. *Phys. Rev. B* **1994**, *50*, 17953−17979.

(60) Kresse, G.; Joubert, D. From Ultrasoft Pseudopotentials to the Projector Augmented-Wave Method. *Phys. Rev. B* **1999**, *59*, 1758−1775.

(61) Perdew, J. P.; Burke, K.; Ernzerhof, M. Generalized Gradient Approximation Made Simple. *Phys. Rev. Lett.* **1996**, *77*, 3865−3868.

(62) Nosé, S. A Unified Formulation of the Constant Temperature Molecular Dynamics Methods. *J. Chem. Phys.* **1984**, *81*, 511−519.

(63) Nosé, S. Constant Temperature Molecular Dynamics Methods. *Prog. Theor. Phys. Suppl.* **1991**, *103*, 1−46.

(64) Bylander, D. M.; Kleinman, L. Energy Fluctuations Induced by the Nosé Thermostat. *Phys. Rev. B* **1992**, *46*, 13756−13761.

(65) Zhu, Z.; Deng, Z.; Chu, I.-H.; Radhakrishnan, B.; Ping Ong, S. *Computational Materials System Design*; Shin, D.; Saal, J., Eds.; Springer International Publishing, 2018; pp 147−168.

(66) Piovano, A.; Perrichon, A.; Boehm, M.; Johnson, M. R.; Paulus, W. Positional Recurrence Maps, a Powerful Tool to De-Correlate Static and Dynamical Disorder in Distribution Maps From Molecular Dynamics Simulations: The Case of Nd_2NiO_{4+d}. *Phys. Chem. Chem. Phys.* **2016**, *18*, 17398−17403.

(67) Hempelmann, R. *Quasielastic Neutron Scattering and Solid State Diffusion*; Clarendon Press: Oxford, 2000.

(68) Gomez, M. A.; Griffin, M. A.; Jindal, S.; Rule, K. D.; Cooper, V. R. The Effect of Octahedral Tilting on Proton Binding Sites and Transition States in Pseudo-Cubic Perovskite Oxides. *J. Chem. Phys.* **2005**, *123*, No. 094703.

(69) Kreuer, K. D.; Münch, W.; Traub, U.; Maier, J. On Proton Transport in Perovskite-Type Oxides and Plastic Hydroxides. *Ber. Bunsenges. Phys. Chem.* **1998**, *102*, 552−559.

(70) Münch, W.; Seifert, G.; Kreuer, K. D.; Maier, J. A Quantum Molecular Dynamics Study of the Cubic Phase of $BaTiO_3$ and $BaZrO_3$. *Solid State Ionics* **1997**, *97*, 39−44.

(71) Chudley, C. T.; Elliott, R. J. Neutron Scattering From a Liquid on a Jump Diffusion Model. *Proc. Phys. Soc.* **1961**, *77*, 353−361.

(72) Hall, P. L.; Ross, D. K. Incoherent Neutron Scattering Functions for Random Jump Diffusion in Bounded and Infinite Media. *Mol. Phys.* **1981**, *42*, 673−682.

(73) Braun, A.; Duval, S.; Ried, P.; Embs, J.; Juranyi, F.; Strässle, T.; Stimming, U.; Hempelmann, R.; Holtappels, P.; Graule, T. Proton Diffusivity in the $BaZr_{0.9}Y_{0.1}O_{3-\delta}$ Proton Conductor. *J. Appl. Electrochem.* **2009**, *39*, 471−475.

(74) Matzke, T.; Stimming, U.; Karmonik, C.; Soetratmo, M.; Hempelmann, R.; Güthoff, F. Quasielastic Thermal Neutron Scattering Experiment on the Proton Conductor $SrCe_{0.95}Yb_{0.05}H_{0.02}O_{2.985}$. *Solid State Ionics* **1996**, *86−88*, 621−628.

(75) Hempehnann, R.; Karmonik, C.; Matzke, T.; Cappadonia, M.; Stimming, U.; Springer, T.; Adams, M. Quasielastic Neutron Scattering Study of Proton Diffusion in $SrCe_{0.95}Yb_{0.05}H_{0.02}O_{2.985}$. *Solid State Ionics* **1995**, *77*, 152−156.

(76) Karmonik, C.; Hempelmann, R.; Cook, J.; Güthoff, F. Investigation of the Proton Migration Mechanism in the Perovskite

Proton Conductor $Ba_3Ca_{1.18}Nb_{1.82}H_{0.2}O_{8.83}$ by Means of Quasielastic Neutron Scattering. *Ionics* **1996**, *2*, 69−74.

(77) Pionke, M.; Mono, T.; Schweika, W.; Springer, T.; Schober, H. Investigation of the Hydrogen Mobility in a Mixed Perovskite: $Ba[Ca_{(1+x)/3}Nb_{(2-x)/3}]O_{3-x/2}$ by Quasielastic Neutron Scattering. *Solid State Ionics* **1997**, *97*, 497−504.

(78) Wilmer, D.; Seydel, T.; Kreuer, K.-D. Proton Diffusion in Hydrated Acceptor-Doped Barium Zirconate. *MRS Online Proc. Libr.* **2007**, *972*, No. 104.

(79) Chen, Q.; Banyte, J.; Zhang, X.; Embs, J. P.; Braun, A. Proton Diffusivity in Spark Plasma Sintered $BaCe_{0.8}Y_{0.2}O_{3-\delta}$: In-Situ Combination of Quasi-Elastic Neutron Scattering and Impedance Spectroscopy. *Solid State Ionics* **2013**, *252*, 2−6.

(80) Wakamura, K. Roles of Phonon Amplitude and Low-Energy Optical Phonons on Superionic Conduction. *Phys. Rev. B* **1997**, *56*, 11593−11599.

(81) Fluri, A.; Gilardi, E.; Karlsson, M.; Roddatis, V.; Bettinelli, M.; Castelli, I. E.; Lippert, T.; Pergolesi, D. Anisotropic Proton and Oxygen Ion Conductivity in Epitaxial $Ba_2In_2O_5$ Thin Films. *J. Phys. Chem. C* **2017**, *121*, 21797−21805.

(82) Yamazaki, Y.; Hernandez-Sanchez, R.; Haile, S. M. High Total Proton Conductivity in Large-Grained Yttrium-Doped Barium Zirconate. *Chem. Mater.* **2009**, *21*, 2755−2762.

(83) Zhang, G. B.; Smyth, D. M. Protonic Conduction in $Ba_2In_2O_5$. *Solid State Ionics* **1995**, *82*, 153−160.

(84) Animitsa, I. E.; Kochetova, N. A.; Shaikhlislamova, A. R. Electric and Thermogravimetric Properties of Brownmillerites Based on Barium Oxides. *Russ. J. Electrochem.* **2007**, *43*, 708−713.

(85) Tyagi, D.; Shirsat, A. N.; Saha, B.; Varma, S. Phase Stabilisation, Chemical Behaviour and Protonic Conductivity of Vanadium Doped Barium Indate for ITSOFC Application. *J. Alloys Compd.* **2021**, *877*, No. 160298.

(86) Lavén, R.; Häussermann, U.; Perrichon, A.; Andersson, M. S.; Targama, M. S.; Demmel, F.; Karlsson, M. Diffusional Dynamics of Hydride Ions in the Layered Oxyhydride $SrVO_2H$. *Chem. Mater.* **2021**, *33*, 2967−2975.

(87) Quarez, E.; Noirault, S.; Caldes, M. T.; Joubert, O. Water Incorporation and Proton Conductivity in Titanium Substituted Barium Indate. *J. Power Sources* **2010**, *195*, 1136−1141.

(88) Jarry, A.; Quarez, E.; Kravchyk, K.; Joubert, O. Rare Earth Effect on Conductivity and Stability Properties of Doped Barium Indates as Potential Proton-Conducting Fuel Cell Electrolytes. *Solid State Ionics* **2012**, *216*, 11−14.

(89) Karlsson, M.; Perrichon, A.; Koza, M. M.; Fouquet, P.; Frick, B. *Experimental Data on $Ba_2In_2O_5(H_2O)_x$ Measured at the ILL* 2016 DOI: 10.5291/ILL-DATA.7-03-152.